mater.scichina.com link.springer.com

Published online 29 November 2025 | https://doi.org/10.1007/s40843-024-3189-1
*Sci China Mater* 2025, 68(1): 156–164

# Unraveling the colloidal composition of perovskite precursor solutions and its impact on film formation

Tiantian Lou[1†], Letian Chen[1†], Guichun Yang[1], Peng Chen[1], Wenyan Zhao[2], Hongshi Li[1*] and Guoran Li[1]

**ABSTRACT** **Colloids are a vital component of perovskite precursor solutions (PPSs), significantly influencing the quality of perovskite film formation. Despite their importance, a comprehensive understanding of these colloids remains elusive. In this work, we explored the colloidal compositions of two distinct PPS types: the monomer-mixing dissolution (MMD) and the pre-synthesized perovskite single crystal redissolution (SCR). We have uncovered a new dissolution chemical equilibrium mechanism where the transition from mixed monomers to the 3C cubic phase (α-phase) involves a reversible transformation. Our findings indicate that although colloidal size significantly affects the nucleation during perovskite crystallization, the composition of the colloids plays a more crucial role. The MMD method yields poly Pb-I·solvent clusters while the colloids derived from the SCR approach produce hexagonal lead-halide-based perovskite phase clusters. These divergent colloidal compositions lead to markedly different impacts on the perovskite film formation process. Notably, hexagonal-phase colloids act as favorable nucleation sites, promoting the generation of the α-phase perovskite films with larger grains, more homogeneous phases, and fewer defects. This work demonstrates the importance of tailoring colloidal compositions and provides theoretical insights into the beneficial effects of redissolving perovskite in forms such as powder, microcrystals, and single crystals.**

**Keywords:** perovskite precursor solutions, colloids, hexagonal-phase colloids, poly Pb-I·solvent clusters, perovskite solar cells

## INTRODUCTION

Perovskite solar cells (PSCs) have attracted widespread attention as promising candidates for next-generation photovoltaic applications due to their low cost, straightforward fabrication process, and remarkable power conversion efficiency (PCE) exceeding 26% [1–5]. Solution processing is a predominant method for fabricating perovskite light-absorbing films, encompassing a range of methods including one-step spin coating, sequential deposition, spray-coating, inkjet printing, blade-coating, and slot-die coating [6–8]. Therefore, a thorough understanding of the chemical properties of perovskite precursor solutions (PPSs) is essential for optimizing the quality of perovskite films and enhancing the performance of the resultant PSCs.

PPSs are characterized by a variety of chemical reactions and complex coordination dynamics, encompassing the cationic side reactions, the solvation of Pb-I, and the colloidal chemistry [9,10]. Reactions involving A-site cations include deprotonation ($MA^+$ to $MA^0$) and condensation processes that yield byproducts such as $MFA^+$, $DMFA^+$ and triazine, among others [11–13]. Additionally, solvent interactions can accelerate the aging of A-site cations, especially in the presence of trace amounts of hydrous DMF solvent [14,15]. In addition, Radicchi et al. revealed that the coordination number and composition of solvated iodoplumbate $[PbI_mX_n]^{2-m}$ complexes, while the Pb-I in the precursor interacts with the double-bonded oxygen in the solvent [16]. It is important to note that their study was conducted in dilute solutions. As the concentration of PPS increases, colloidal formation becomes significant and critical affecting the coverage, orientation, and purity of the resulting perovskite films [17]. However, researchers hold differing views regarding the colloids in PPSs. Kim *et al.* discovered that the colloidal properties of PPSs are directly correlated with the defect concentration and crystallinity of perovskite films, noting that the addition of $I_3^-$ reduces colloid size, facilitating the formation of higher-quality films through the generation of high-valent iodoplumbates [18]. Boonmongkolras *et al.* found colloid intermediates produced by aging PPSs degraded the phase purity of the resultant films and led to poor device performance [19]. Wu *et al.* employed 2-methoxyethanol to produce highly uniform, small-sized colloids, thereby facilitating the homogeneous nucleation and rapid crystallization of perovskite films [20]. Filtering PPSs before use is also a common practice used to remove insoluble impurities and colloids. Conversely, according to classical LaMer nucleation theory, large-sized colloids acting as nucleation sites can significantly reduce the energy barrier for nucleation, facilitating the formation of high-quality α-phase perovskite films [21]. Thus, deepening our understanding and precise tailoring of colloids in PPSs is crucial for further enhancing the resultant film quality.

The employment of large-sized colloids to enhance perovskite film formation is typically linked to strategies involving the redissolution of pre-synthesized perovskite crystals [22]. Pre-synthesized δ-phase yellow and α-phase black $FAPbI_3$ powders, microcrystals, and single crystals, produced via mechanochemistry and wet chemistry methods, not only enhance the

[1] School of Materials Science and Engineering, Institute of New Energy Material Chemistry, Renewable Energy Conversion and Storage Center, Nankai University, Tianjin 300350, China
[2] School of Mechanical and Electronic Engineering, Jingdezhen Ceramic University, Jingdezhen 333403, China
[†] Equally contributed to this work.
[*] Corresponding author (email: lhs_kls@nankai.edu.cn)

 © Science China Press 2024 

purity and achieve precise stoichiometric ratios but also form larger colloids within the PPSs [21,23–25]. This strategy facilitates preferable crystallization through spontaneous nucleation, preferred crystal orientations, and reduced carrier trap states in the resulting perovskite films. Besides, Fei *et al.* discovered that perovskite microcrystals for preparing PPS can improve the long-term stability of the PPS and the perovskite film [26]. Redissolving pre-synthesized perovskites offers a promising avenue for boosting the performance of PSCs, dependent on a deeper understanding of the colloidal chemistry within the PPSs.

Herein, we investigate for the first time the colloidal compositions of two distinct PPS types: the conventional monomer-mixing dissolution (MMD) and the pre-synthesized perovskite single crystal redissolution (SCR). The MMD method yields soft $x$FAI·$y$PbI$_2$·solvent clusters (where $x < y$), characterized as poly Pb-I·solvent clusters. In contrast, the colloids derived from the SCR approach produce hexagonal lead-halide-based perovskite phase clusters. We have uncovered a new dissolution chemical equilibrium mechanism where the transition from mixed monomers to the 3C cubic phase (α-phase) involves a reversible transformation from poly Pb-I·solvent clusters to hexagonal phases (2H (δ phase), 4H, and 6H FAPbI$_3$). These divergent colloidal compositions lead to markedly different impacts on the perovskite film formation process. Our findings indicate that the colloids in the MMD are unfavorable for obtaining high-quality perovskite films due to their composition, whereas the presence of hexagonal-phase colloids in the SCR acts as favorable nucleation sites and promotes the generation of the α-phase, resulting in perovskite films with larger grain sizes, more homogeneous phases and lower densities of trap states. Moreover, hexagonal-phase colloids can inhibit the cationic side reactions in aging precursor, enhancing the long-term stability of the PPS. Ultimately, a PCE of 23.5% was achieved for PSC based on SCR, featuring an improved open-circuit voltage ($V_{OC}$) and better stability compared to that of MMD.

## EXPERIMENTAL SECTION

### Synthesis of α-$FA_{0.94}MA_{0.06}Pb(I_{0.94}Br_{0.06})_3$ single crystals

73.32, 73.32, 4.68 and 4.68 mM of PbI$_2$, FAI, MABr and PbBr$_2$ were dissolved in GBL (78 mM) overnight and filtered using PTFE filters with a 0.22 μm pore size. Then the glass petri dish containing the perovskite solution was placed in the oven. The specific synthesis of perovskite single crystal was adjusted according to the reported literature [27]. Finally, the single crystals were removed from the solution, and the remaining solvent was repeatedly blotted out with filter paper, then the single crystals were vacuum dried in a vacuum oven for 3 h and placed in a glove box.

### Device fabrication

Fluorine-doped tin oxide (FTO) conductive glasses were cleaned using a detergent aqueous solution, acetone, and anhydrous ethanol by sonicating for 40 min for each step. The SnO$_2$ electron transport layer was prepared by chemical water bath deposition (CBD) method. Before depositing the SnO$_2$ layer, FTO/glass substrates were treated with ultraviolet (UV)-ozone for 15 min. The FTO glass was then placed into a solution prepared by dissolving 275 mg $SnCl_2$-$2H_2O$, 1250 mg urea $(NH_2)_2CO$, 0.025 mL of mercaptoacetic acid and 1.25 mL of hydrochloric acid into 100 mL of deionised water, then placed in a 94°C water bath for 5.5 h for deposition. Afterward, the SnO$_2$-coated substrates were treated with UV-ozone for 20 min and transferred into an $N_2$ glove box. The perovskite films were fabricated via the one-step antisolvent method. The control perovskite precursor solution was prepared by mixing 1.4 M PbI$_2$, 1.4 M FAI and 0.09 M PbBr$_2$ and 0.09 M MABr powder in DMF and DMSO (8:1, v/v). For the SC perovskite solution preparation, the synthesized α-$FA_{0.94}MA_{0.06}Pb(I_{0.94}Br_{0.06})_3$ single crystals were used to replace the powder mixture in 1.4 M precursor. All perovskite precursor solutions contained 35 mol% MACl and 4 mol% excess PbI$_2$. The perovskite film was deposited by spin coating at 1000 and 5000 r min$^{-1}$ for 10 and 30 s respectively. 120 μL of CB was dripped on the spinning substrate at the 25th second. Then the fresh film was annealed at 150°C for 15 min in the air. After cooling down to room temperature, 1 mg mL$^{-1}$ of Octylammonium bromide (OABr) dissolved in IPA was spin-coated on top of the perovskite film at 3500 r min$^{-1}$ for 30 s. The hole transfer materials were deposited on the perovskite film at 3500 r min$^{-1}$ for 30 s, prepared by dissolving 85.78 mg Spiro-OMeTAD, 35 μL Li-TFSI solution (520 mg mL$^{-1}$ in ACN), 12 μL Co-TFSI solution (300 mg mL$^{-1}$ in ACN), 39 μL TBP into 1 mL CB. Finally, 60 nm of the gold electrode was thermally evaporated in an ultra-high-vacuum chamber integrated inside the glovebox.

### Characterizations

Field-emission scanning electron microscopy (SEM, JSM-7800F) was used to investigate the surficial and cross-sectional morphology, with an accelerating voltage of 15 kV. Dynamic light scattering (DLS) spectra are performed on wide-angle laser scattering detectors (ZETAPALS/BI-200SM). Analysis of elemental concentrations in precursor fluids were measured at inductively coupled plasma optical emission spectrometer (ICP-OES) (ThermoFisher iCAP7400). Proton nuclear magnetic resonance spectroscopy ($^1$H NMR) spectra are recorded using Bruker 400 M. The UV-visible (UV-vis) absorption spectroscopy of the perovskite films and precursor solution were measured using the spectrophotometer (Agilent Cary 100). The steady-state photoluminescence (PL) and time-resolved PL (TRPL) were performed on an Edinburgh Instruments FLS5 spectrofluorometer (Edinburg, UK) additionally equipped with an integrating sphere. All PL-related tests were measured under the excitation wavelength of 475 nm. Atomic force microscopy (AFM) and Kelvin probe atomic force microscope (KPFM) of perovskite films were performed with atomic force microscope (Dimension Icon). The X-ray diffraction (XRD) samples were characterized by theta-theta type X-ray diffractometer (Rigaku, Japan). The photocurrent-voltage ($J$-$V$) characteristics of the solar cells with an active area of 0.09 cm$^2$ were measured using a Keithley 2450 Source Meter under illumination of a simulated sunlight (AM1.5, 100 mW cm$^{-2}$) using a 150 W Class AAA solar simulator (Oriel Sol3A 94023A). The sweeping conditions are: reverse scan (1.20 V → −0.05 V, scan rate 0.1 V s$^{-1}$, and no delay time) and forward scan (−0.05 V → 1.20 V, scan rate 0.1 V s$^{-1}$, and no delay time). The light intensity was calibrated by a standard monocrystalline silicon diode with a 91150-KG5 filter before test. The standard monocrystalline silicon reference cell was calibrated in March 2021 at PV Metrology Laboratory of NIM (National Institute of Metrology, China). The $J$-$V$ measurements of solar cells were performed in ambient air and without any encapsulation. All the tested perovskite films were

 © Science China Press 2024 

prepared onto FTO/$SnO_2$ substrates according to the device fabrication method mentioned above.

## RESULTS AND DISCUSSION

We directly synthesized high-quality di-cationic mixed halide $FA_{0.94}MA_{0.06}Pb(I_{0.94}Br_{0.06})_3$ perovskite single crystals following the inverse temperature crystallization method previously reported (see Experimental Section for details) [27]. The XRD results show that centimeter-scale black single crystals, predominantly in the 3C phase perovskite with tiny 2H phase, maintain stability after aging for 3600 h, as demonstrated in Fig. 1a. The typical Tyndall scattering is observed when projecting a 532 nm wavelength laser beam on the PPSs based on MMD and SCR approach, suggesting the presence of colloidal dispersions instead of true solutions (Fig. S1). DLS test was carried out to assess the diameter distribution of both precursor solutions. As shown in Fig. 1b, c, both precursors feature colloidal particles ranging from ~2 nm to several hundred or thousand nanometers. Notably, colloidal sizes within the SCR strategy are significantly larger, potentially facilitating the nucleation process for perovskite film formation. We also assessed the impact of filtration on the colloids in the PPSs (Fig. S2); after filtration, the larger colloids are removed, leaving primarily small colloidal particles around 2 nm. Hereafter, "C-Filtered" will denote the filtered control precursor, "C-Unfiltered" the unfiltered control, "S-Filtered" the filtered precursor from SCR, and "S-Unfiltered" the unfiltered SCR precursor.

To investigate the colloidal composition of the precursors obtained from the MMD and SCR, inductively coupled plasma emission spectroscopy (ICP-OES) was carried out and the obtained emission intensities of Pb and I in different precursor solutions were shown in Fig. 1d and Table S1. The test results show that the Pb intensity in the S-Filtered precursor decreased by 8.27% compared to the S-Unfiltered precursor, while in the C-Filtered, it decreased by only 3.69% compared to the C-Unfiltered. This suggests that the colloids obtained through the SCR contain a higher concentration of lead content relative to those from the MMD. On the other hand, for the MMD precursor, the iodine concentration unexpectedly increased after filtration, indicating that the colloids in MMD precursor contain solvent-coordinated complex where a portion of iodine is replaced by double-bonded oxygen [10,16]. The thickness of the resultant perovskite films, correlating with the concentration of different PPSs, is also illustrated in Fig. S3.

Furthermore, we calculated the intensity ratio of I and Pb (I/Pb) in the four different solutions (Fig. 1e). For MMD, C-Filtered exhibits a higher I/Pb ratio than C-Unfiltered, indicating stoichiometric differences between colloids and true solutions. We hypothesize that the colloids in the MMD precursor consist of a series of iodoplumbate complexes, acting as building blocks for the self-assembly of poly (lead iodide) frameworks. In the presence of solvation, Pb-I interacts with double-built oxygen to form Pb–O coordination. Consequently, the colloids in the MMD precursor likely take the form of $x$FAI·$y$PbI$_2$·solvent ($x < y$), which deviates from the stoichiometric ratio of perovskite. However, for SCR, S-Filtered exhibits a similar I/Pb ratio to S-Unfiltered, suggesting that the stoichiometric ratio remains nearly unchanged after removing colloids. This implies that the composition of colloids in the SCR precursor is likely perovskite. It was hypothesized that by dissolving the perovskite single crystals (3C) directly in the solvent, the 3C-phase perovskite did not dissolve to form poly Pb-I·solvent clusters, but rather existed in the form of hexagonal lead-halide-based perovskites, especially, the 2H, 4H, and 6H phases of $FAPbI_3$ [28].

$^1$H-NMR was conducted to investigate cationic side reactions in C-Unfiltered and S-Unfiltered precursors aged for 5 days, as

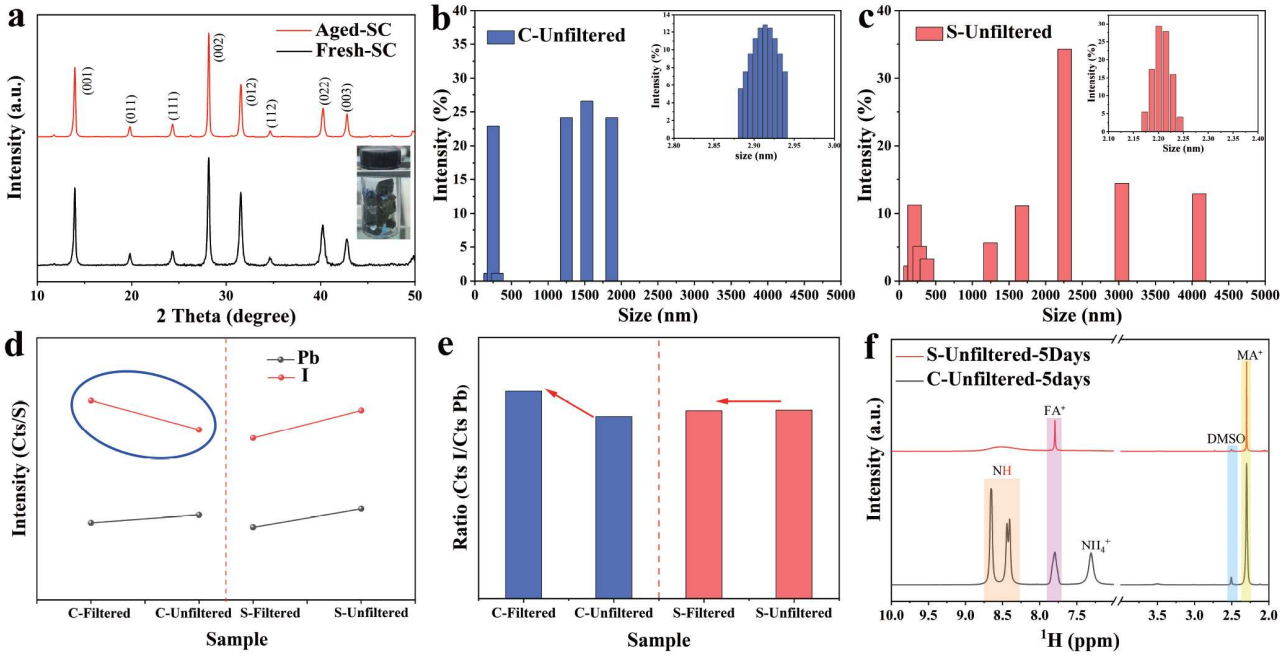


**Figure 1** (a) XRD pattern of fresh and aged perovskite single crystals. The inset is a photograph of synthesized perovskite single crystals. (b, c) DLS results of the perovskite precursors using MMD (denoted as C-Unfiltered) and synthesized perovskite single crystal (denoted as S-Unfiltered), respectively. The insets represent the distribution of small-sized colloids in the range of a few nanometers in the C-Unfiltered and S-Unfiltered precursors, respectively. (d, e) ICP-OES results of C-Filtered, C-Unfiltered, S-Filtered and S-Unfiltered. (f) $^1$H NMR spectra of C-Unfiltered and S-Unfiltered perovskite precursors aged for 5 days.


© Science China Press 2024

shown in Fig. 1f. The aging C-Unfiltered precursor exhibited peaks indicative of $NH_4^+$ byproducts and the broadening of the $FA^+$ peaks [14,29,30]. The $^1H$ NMR spectra of MACl and FAI in DMSO-$d_6$ are presented in Figs S4 and S5, respectively. NMR integration, using the solvent peaks as a reference, suggested a relative decrease in the $FA^+$ and $MA^+$ peak areas for C-Unfiltered, implying the occurrence of more side reactions (Fig. S6). On one hand, monomer reagent impurities in the MMD approach can catalyze PPS degradation more than the high-purity perovskite single crystals used in the SCR precursor [31]. More importantly, the hexagonal-phase colloids of the SCR precursor reduce molecular collision probability by isolating the cations, whereas the MMD approach promotes cation collisions. These cation collisions in the C-Unfiltered precursor led to stronger intermolecular interactions, such as hydrogen bonding between FA cations, resulting in the broadening of the $FA^+$ signal.

To investigate the colloidal composition and the interfacial stability of perovskite phases in solvent, we carried out ab-initio molecular dynamics (AIMD) simulations to assess the formation energy of five surfaces ($2H_{100}$, $2H_{101}$, $4H_{100}$, $4H_{101}$, and $3C_{100}$) in DMSO/DMF solvent mixture (details of computational methods and analysis are presented in the Supplementary Information and Videos S1–S5). These interface models and DMSO/DMF solvent mixture underwent sufficiently long AIMD simulations to ensure equilibrium, as indicated by stable atomic energies over the final 5 ps (Figs S7–S10). Interface energies were determined by conducting statistical analysis on this stable energy data, yielding the respective mean energies and standard deviations, as shown in Fig. 2a and Table S2. According to simulation results, the negative formation energies, ranging from −0.79 to −0.94 eV/atom, indicate that hexagonal perovskite can maintain its structure when exposed to solvents. Among them, $2H_{100}$, $4H_{101}$, and $3C_{100}$ with solvent exhibited relatively negative formation energies, which correlate with the XRD results discussed later. On the other hand, experimentally, we did not observe the presence of 3C phase perovskite colloids in the solution (as indicated by the solution color and UV-vis results (Figs S11 and S12)) [32]. We infer that this is due to the transition from the 3C phase to the hexagonal phase being an entropy-increasing process, whereby the 3C phase spontaneously transitions to the hexagonal phase under the influence of solvent.

As shown in Fig. 2b, c, we have proposed a new dissolution chemical equilibrium mechanism where the transition from mixed monomers to the 3C phase involves a reversible transformation from poly Pb-I·solvent clusters to hexagonal phases. Lead iodide octahedra also undergo reversible transitions among edge-sharing, face-sharing, and corner-sharing configurations. Further, we have inferred the colloidal compositions of both the MMD and SCR precursors. Upon addition of monomer raw materials FAI and $PbI_2$ etc. into the solvent (DMF/DMSO), poly Pb-I·solvent clusters are formed through a series of solvation and coordination interactions. The I/Pb ratio suggests that poly Pb-I·solvent clusters are predominant in colloids, indicating a significant energy barrier from poly Pb-I·solvent clusters to hexagonal phase perovskite colloids. When 3C perovskite single crystals are used as precursors, a phase transition occurs from the 3C phase transforming into the hexagonal phases, predominantly forming 2H/4H phase colloids [32].

To further explore the colloidal composition within PPSs and its impact on the resultant perovskite films, we conducted a series of experiments to track the transformation of intermediate phases from PPSs to wet films/films, as illustrated in Fig. 3. The simulated XRD results for the 2H, 4H, and 6H phase perovskites are displayed in Fig. S13 [28]. Firstly, we spread the MMD and SCR precursors on the glass substrates and evaporated the solvents through annealing; the XRD results are displayed in Fig. 3a. Compared to the C-Unfiltered film, the S-Unfiltered film exhibits stronger $3C_{100}$ peaks and weaker $2H_{100}$ peaks, while also displaying significant 4H phase peaks around 12.7° ($4H_{101}$) and 29°. This indicates that the colloids in SCR may contain the 4H phase, which further promotes the formation of the 3C-phase perovskite films. Within a few minutes of exposure to ambient air, the black films turned yellow, with the 4H peak disappearing and the 3C peak decreasing for S-Unfiltered, thereby eliminating the misleading signals from $PbI_{2(001)}$ (Fig. 3b). Meanwhile, the color transition in C-Unfiltered films was more rapid, marked by a swift shift to the 2H phase.

Then, we investigated the film-forming intermediates using spin-coating, under conditions with and without anti-solvent and annealing. Wet films, obtained by spin-coating PPSs without anti-solvent or annealing, are analyzed in the XRD results shown in Fig. 3c. The intensity of solvate phase peaks is higher in the C-Unfiltered film than in the S-Unfiltered film, indicating a greater presence of solvated clusters in the MMD precursor [33,34]. In addition, the 2H phase peaks of S-Unfiltered film are almost negligible, whereas 6H intermediate and 3C perovskite phase peaks are more distinct than those in C-Unfiltered film. This suggests the presence of colloids composed of perovskite intermediate phase in the S-Unfiltered precursor and they facilitate the rapid transition from 2H to 4H to 6H and 3C phases during the spontaneous nucleation and crystallization of perovskite. The XRD patterns of C-Filtered and S-Filtered exhibit similar solvation peaks, indicating the presence of solvation by small-sized colloids, along with a higher proportion of the 2H phase relative to the 6H and 3C phases (Fig. S14). Wet films of C-Unfiltered, C-Filtered, S-Unfiltered, and S-Filtered, obtained by spin-coating PPSs with anti-solvent and without annealing, are analyzed in the XRD results depicted in Fig. 3d, e. On one hand, the films from all four precursors exhibit a strong $6H_{(101)}$ peak and a weak $3C_{(001)}$ peak. The intensity ratios of $3C_{(001)}/6H_{(101)}$, which indicate the degree of phase transition completion, are 40.3%, 44.1%, 63.1%, and 51.3% for C-Unfiltered, C-Filtered, S-Unfiltered, and S-Filtered, respectively. Notably, S-Unfiltered films demonstrate a much faster phase transition to the 3C phase than others, suggesting that the presence of larger hexagonal colloids accelerates spontaneous crystallization. On the other hand, the analysis of peak intensities for 2H, 6H, and 3C in the MMD-derived C-Unfiltered and C-Filtered films suggests that poly Pb-I·solvent cluster colloids may induce heterogeneous phases, adversely affecting the quality of perovskite films and the performance of photovoltaic devices.

The XRD results of perovskite films formed under normal conditions are displayed in Fig. 3f, showing similar XRD patterns for both C-Unfiltered and S-Unfiltered films, with the exception of some heterogeneities in the C-Unfiltered films. We applied the Williamson-Hall method to extract lattice aberrations from the XRD patterns [35]. As depicted in Fig. S16, lattice distortion is indicated by the slope of the fitted line, which is higher for the C-Unfiltered film ($\varepsilon$ = 0.114%) compared to the S-Unfiltered film ($\varepsilon$ = 0.073%), suggesting that perovskite films

 © Science China Press 2024 

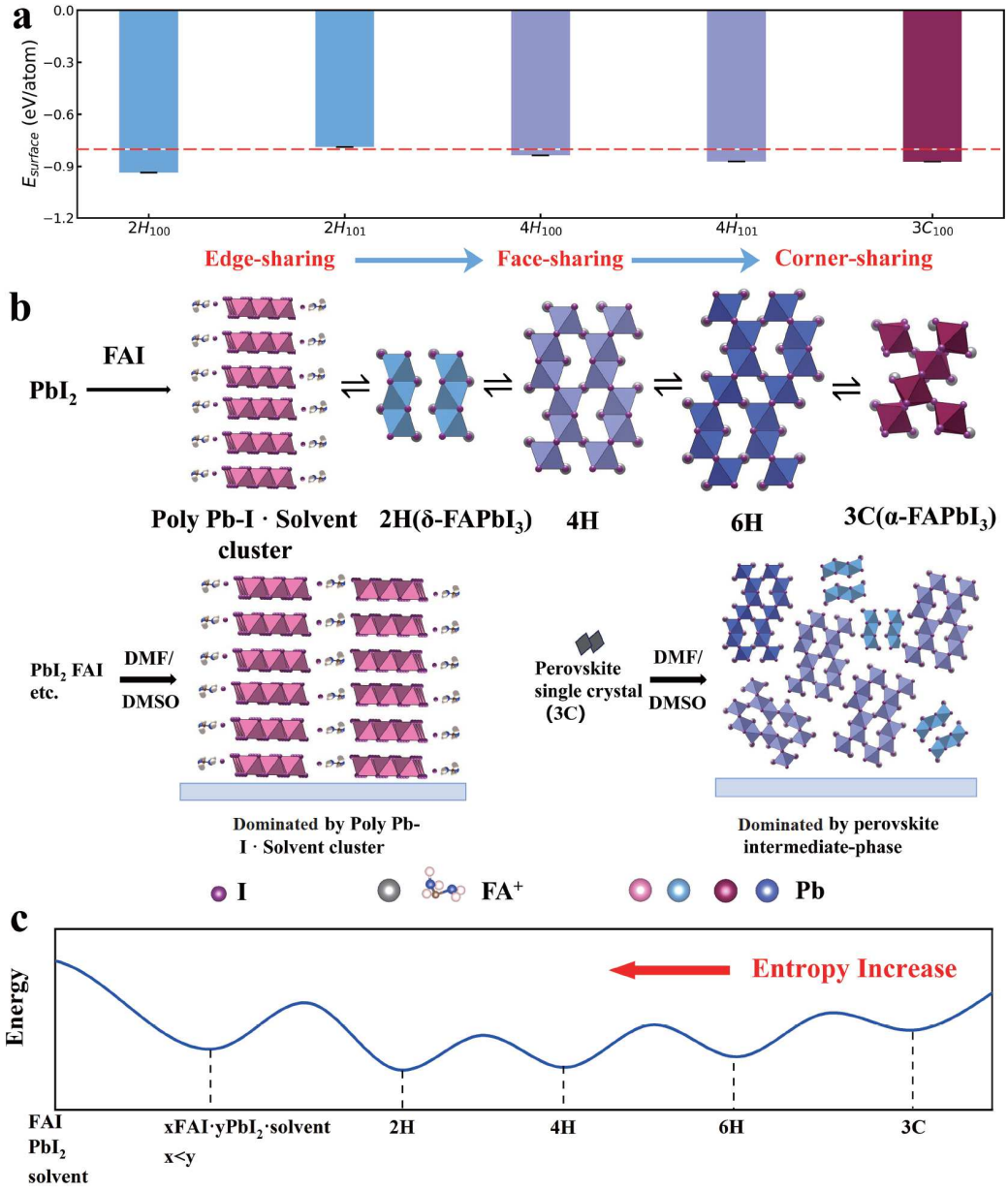


**Figure 2** (a) Formation energies of the five surfaces ($2H_{100}$, $2H_{101}$, $4H_{100}$, $4H_{101}$, and $3C_{100}$) in DMSO/DMF solvent mixtures determined by AIMD. (b) Schematic diagram of the chemical equilibrium relationships for dissolution processes and the colloidal composition of precursors of MMD and SCR. (c) The energy schematic diagram of perovskite different phases.

from the SCR approach exhibit less lattice distortion. The results from the aforementioned XRD analysis demonstrate that hexagonal-phase colloids, as opposed to poly Pb-I·solvent clusters in PPSs, more effectively promote the transformation into the perovskite 3C phase during film formation.

The properties of perovskite films corresponding to the MMD and SCR methods have been further explored. As depicted in Fig. 4a–d, top-view SEM tests were conducted to characterize the surface morphology of the perovskite films. Additionally, Fig. S15 illustrates the grain size distribution statistics obtained via SEM. The average grain sizes of S-Unfiltered and C-Unfiltered, at 0.80 and 0.58 μm respectively, are larger compared to those of S-Filtered and C-Filtered, which are 0.48 and 0.47 μm respectively. This increase in grain size can be attributed to the effect of colloids in the PPSs. However, C-Unfiltered films exhibit many small grains interspersed with pinholes. In contrast, S-Unfiltered perovskite films not only have the largest average grain size but also show significantly improved film quality with no pin-holes and a smoother surface, also confirmed by atomic force microscopy results (Fig. S17). The surface potential result derived from KPFM (Figs S18 and S19) indicates that the S-Unfiltered and C-Unfiltered perovskite films have similar surface potentials.

To comprehensively assess the impact of colloids on the optoelectronic properties of perovskite films, we conducted detailed studies on carrier transport, recombination kinetics, and defect density in the resulting films and devices. Steady-state PL and TRPL measurements were performed on perovskite films

 © Science China Press 2024 

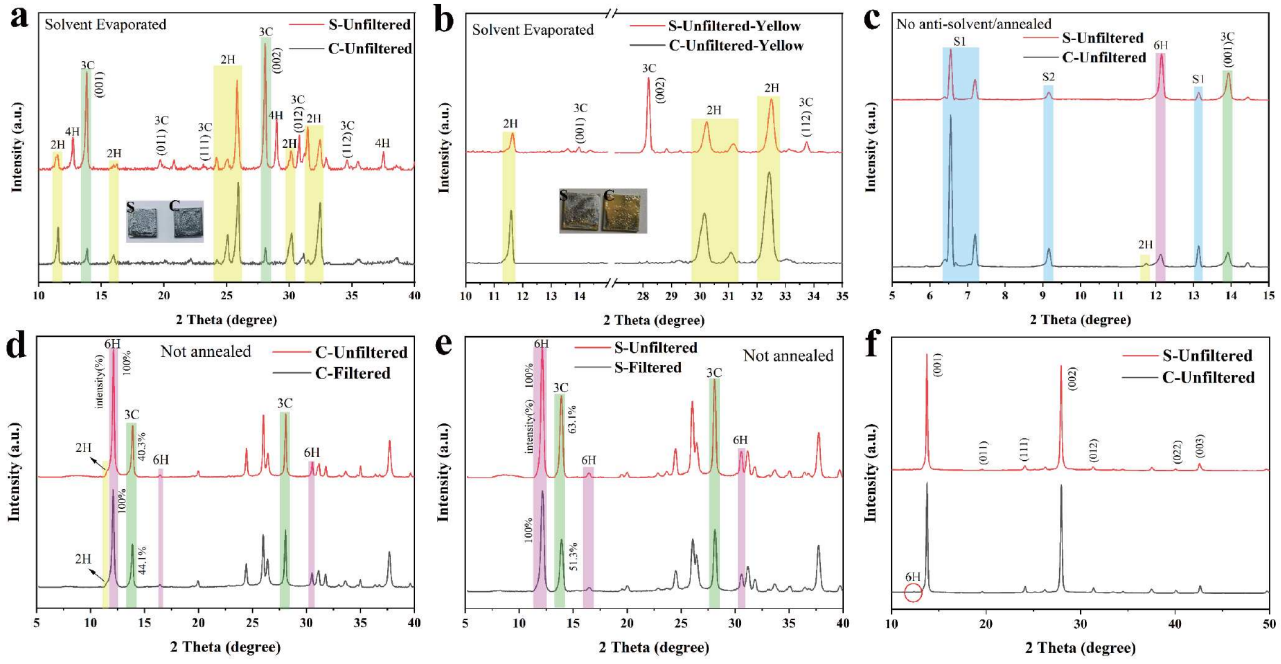


**Figure 3** XRD patterns of resultant perovskite films: (a) prepared by evaporating the solvent directly at 150° for 15 min and (b) after turned yellow in ambient air, and (c) without anti-solvent or annealing. (d, e) XRD pattern of intermediate films with anti-solvent and without annealing. (f) XRD pattern of C-Unfiltered and S-Unfiltered perovskite films under normal treatment.

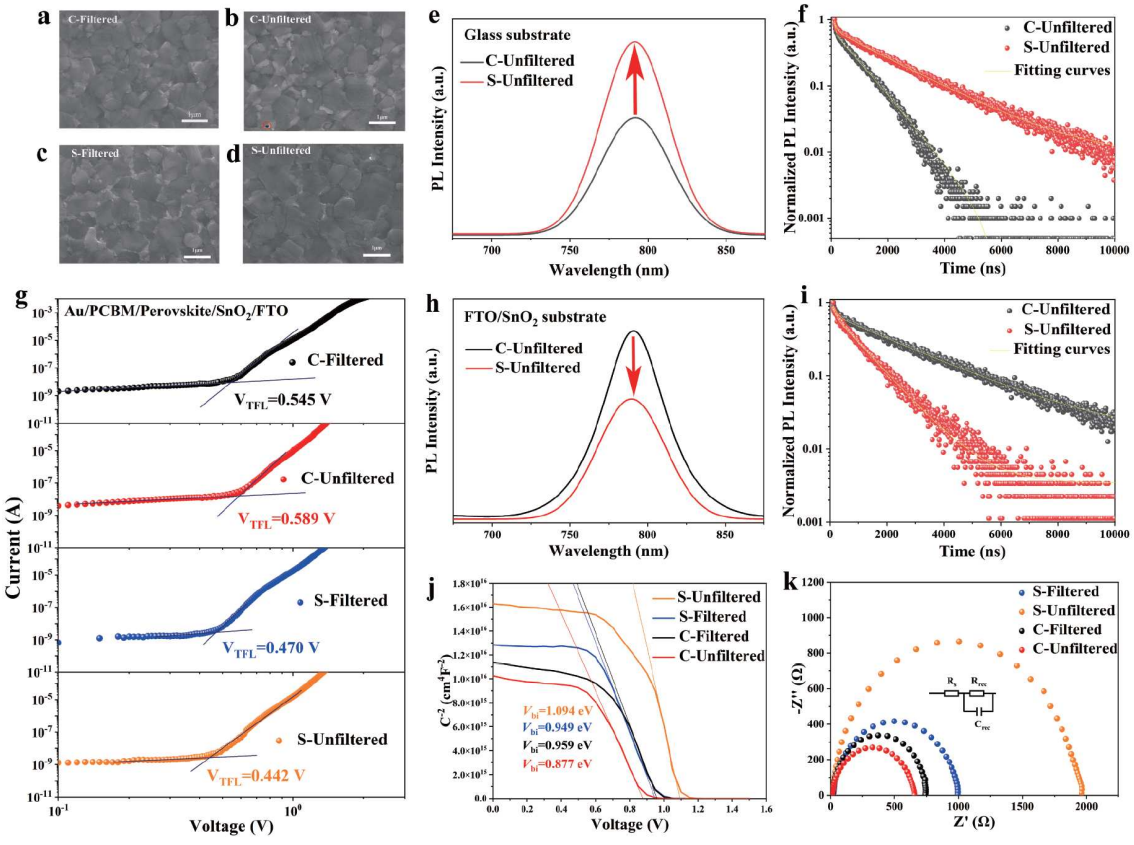


**Figure 4** (a–d) Top-view SEM images of C-Filtered, C-Unfiltered, S-Filtered and S-Unfiltered films. (e) Steady-state PL spectra and (f) TRPL decays of the C-Unfiltered and S-Unfiltered perovskite films deposited on glass substrate. (h) Steady-state PL spectra and (i) TRPL decays of the C-Unfiltered and S-Unfiltered perovskite films deposited on the FTO/$SnO_2$ substrates. (g) SCLC characteristics of electron-only devices. (j) M-S analysis of the devices. (k) EIS of the C-Filtered, C-Unfiltered, S-Filtered, and S-Unfiltered devices measured with a bias of 1.0 V under dark conditions. The inset presents the equivalent circuit model.


© Science China Press 2024

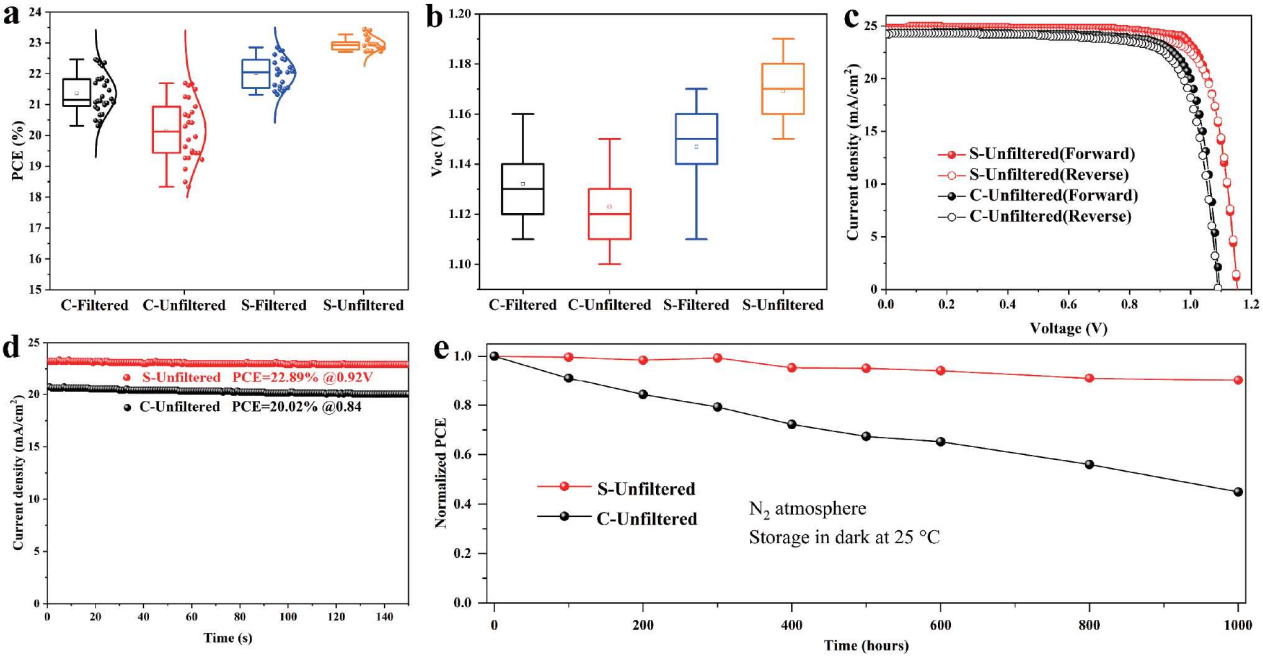


**Figure 5** (a) Statistical distributions of PCEs collected from a batch of 100 devices for the C-Filtered, C-Unfiltered, S-Filtered, and S-Unfiltered devices. (b) $V_{OC}$ distribution of perovskite solar cells. (c) *J-V* curves of the C-Unfiltered and S-Unfiltered devices under both forward and reverse scans. (d) The stabilized power outputs over 150 s of the C-Unfiltered and S-Unfiltered devices were measured at voltages of 0.84 and 0.92 V in the ambient environment, respectively. (e) Dark stability of the unencapsulated devices in the nitrogen environment.

deposited on different substrates (Fig. 4e, f, h, i and Tables S3 and S4). Comparisons of PL intensities and TRPL fitted lifetimes demonstrate that S-Unfiltered films obtained through the SCR approach effectively reduce defect state density, suppress non-radiative carrier recombination, and enhance carrier transport properties. UV-vis and PL spectra (Figs S20 and S21) of the control and single-crystal groups show that single-crystal re-dissolution and filtration operations do not change the bandgap of the perovskite films. Space-charge-limited current (SCLC) tests were carried out to evaluate the trap state density ($N_t$) in perovskite devices (Fig. 4g) [36,37]. The $N_t$ is calculated by using the trap-filled limited voltage ($V_{TFL}$), yielding values of $3.50 \times 10^{15}$, $3.78 \times 10^{15}$, $2.94 \times 10^{15}$, and $2.83 \times 10^{15}$ $cm^{-3}$ for the C-Filtered, C-Unfiltered, S-Filtered, and S-Unfiltered devices, respectively. Mott-Schottky (M-S) analysis revealed built-in potentials ($V_{bi}$) of 0.959, 0.877, 0.949, and 1.094 V for the C-Filtered, C-Unfiltered, S-Filtered, and S-Unfiltered devices, respectively (Fig. 4j). The significantly larger $V_{bi}$ indicates that the S-Unfiltered device has a strong internal drift force for carrier separation and transport. Electrochemical impedance spectroscopy (EIS) results (Fig. 4k) show that S-Unfiltered devices exhibit the highest recombination resistance ($R_{rec}$). The results from the aforementioned optoelectronic characterizations reveal that the presence of poly Pb-I·solvent cluster colloids increases the trap state density in the films, adversely affecting device performance. In contrast, hexagonal-phase colloids in PPSs serve as favorable nucleation sites, facilitating the formation of perovskite films with larger grains, more homogeneous phases, and fewer defects.

We employed a device structure of FTO/$SnO_2$/Perovskite/2D/HTL/Au to assess the performance of perovskite devices. Fig. 5a displays a comparison of the PCE for devices fabricated from different PPSs. The average PCE of the S-Unfiltered device is significantly higher than those of the others and demonstrates the best reproducibility. In contrast, the C-Unfiltered devices show the poorest performance and reproducibility. Besides, the C-Filtered and S-Filtered devices show similar PCE distributions. These findings indicate that both colloidal size and composition need to synergistically interact to enhance the performance of PSCs. Hexagonal colloids are beneficial for forming higher-quality perovskite films, while poly Pb-I·solvent clusters negatively impact their quality. The significantly contrasting $V_{OC}$ further confirms the differences in defects within the films, as depicted in Fig. 5b, consistent with the $V_{bi}$ results.

The current *J-V* curves of typical S-Unfiltered and C-Unfiltered devices are shown in Fig. 5c. The C-Unfiltered device has a PCE of 21.3% while the S-Unfiltered device had a significantly enhanced PCE of 23.5%, with $J_{SC}$ of 24.8 mA $cm^{-2}$, $V_{OC}$ of 1.16 V, and fill factor (*FF*) of 81.9%. Additionally, the stabilized power output efficiency of the devices at the maximum power point is shown in Fig. 5d and Fig. S22. ISOS-Dark-Inert stability tests, depicted in Fig. 5e, present that the efficiency of the C-Unfiltered device decreased to 45% of its initial value after 1000 h, whereas the S-Unfiltered device maintained more than 90% of its initial efficiency under the same conditions, indicating its superior long-term storage stability. Furthermore, a comparison of S-Unfiltered devices using both fresh and 5-month-aged perovskite single crystals revealed similar PCE distributions, as depicted in Fig. S23.

## CONCLUSIONS

In summary, we investigate for the first time the colloidal compositions of MMD and SCR precursors, uncovering a new dissolution chemical equilibrium mechanism that transitions from mixed monomers to the different perovskite phases. We reveal that poly Pb-I·solvent clusters in the MMD precursors are

 © Science China Press 2024 

unfavorable for producing high-quality perovskite films, as they increase the trap state density, adversely affecting device performance. In contrast, the presence of hexagonal-phase colloids in the SCR approach acts as favorable nucleation sites, promoting the generation of the α-phase perovskite films with larger grains, more homogeneous phases, and fewer defects.

**Received 5 September 2024; accepted 8 November 2024; published online 29 November 2024**


1 Kojima A, Teshima K, Shirai Y, *et al.* Organometal halide perovskites as visible-light sensitizers for photovoltaic cells. J Am Chem Soc, 2009, 131: 6050–6051
2 Wei Q, Liang H, Haruta Y, *et al.* From tetragonal to cubic: perovskite phase structure evolution for high-performance solar cells. Sci Bull, 2023, 68: 141–145
3 Zhou J, Tan L, Liu Y, *et al.* Highly efficient and stable perovskite solar cells via a multifunctional hole transporting material. Joule, 2024, 8: 1691–1706
4 Chen H, Liu C, Xu J, *et al.* Improved charge extraction in inverted perovskite solar cells with dual-site-binding ligands. Science, 2024, 384: 189–193
5 Li H, Liu S C. Revolutionary SAMs: transforming inverted perovskite solar cells. J Mater Chem A, 2024, 12: 9929–9932
6 Park NG, Zhu K. Scalable fabrication and coating methods for perovskite solar cells and solar modules. Nat Rev Mater, 2020, 5: 333–350
7 Chen L, Chen L, Chen Z, *et al.* Ionic Bonding Without Directionality Facilitates Efficient Interfacial Bridging for Perovskite Solar Cells. Small, 2024, 20: 2308964
8 Burschka J, Pellet N, Moon S J, *et al.* Sequential deposition as a route to high-performance perovskite-sensitized solar cells. Nature, 2013, 499: 316–319
9 Jung M, Ji S G, Kim G, *et al.* Perovskite precursor solution chemistry: from fundamentals to photovoltaic applications. Chem Soc Rev, 2019, 48: 2011–2038
10 Guo Y, Shoyama K, Sato W, *et al.* Chemical pathways connecting lead(II) iodide and perovskite via polymeric plumbate(II) fiber. J Am Chem Soc, 2015, 137: 15907–15914
11 Wang X, Fan Y, Wang L, *et al.* Perovskite solution aging: What happened and how to inhibit? Chem, 2020, 6: 1369–1378
12 Hu J, Ahn JW, Xu Z, *et al.* Iodine modulates the MACl-assisted growth of $FAPbI_3$ for high efficiency perovskite solar cells. Adv Energy Mater, 2024, 14: 2400500
13 Juarez-Perez E J, Ono L K, Qi Y. Thermal degradation of formamidinium based lead halide perovskites into *sym*-triazine and hydrogen cyanide observed by coupled thermogravimetry-mass spectrometry analysis. J Mater Chem A, 2019, 7: 16912–16919
14 Chen L, Hu M, Risqi A M, *et al.* Unraveling the influence of solvent on side reactions between formamidinium lead triiodide and methylammonium cations. J Am Chem Soc, 2024, 146: 10159–10166
15 Dou B, Wheeler L M, Christians J A, *et al.* Degradation of highly alloyed metal halide perovskite precursor inks: mechanism and storage solutions. ACS Energy Lett, 2018, 3: 979–985
16 Radicchi E, Mosconi E, Elisei F, *et al.* Understanding the solution chemistry of lead halide perovskites precursors. ACS Appl Energy Mater, 2019, 2: 3400–3409
17 Yan K, Long M, Zhang T, *et al.* Hybrid halide perovskite solar cell precursors: colloidal chemistry and coordination engineering behind device processing for high efficiency. J Am Chem Soc, 2015, 137: 4460–4468
18 Kim J, Park B, Baek J, *et al.* Unveiling the relationship between the perovskite precursor solution and the resulting device performance. J Am Chem Soc, 2020, 142: 6251–6260
19 Boonmongkolras P, Kim D, Alhabshi E M, *et al.* Understanding effects of precursor solution aging in triple cation lead perovskite. RSC Adv, 2018, 8: 21551–21557
20 Fang Y, Tian T, Yang M, *et al.* Tailoring precursor chemistry enabled room temperature-processed perovskite films in ambient air for efficient and stable solar cells with improved reproducibility. Adv Funct Mater, 2023, 33: 2303674
21 Zhang Y, Wang Y, Yang X, *et al.* Mechanochemistry advances high-performance perovskite solar cells. Adv Mater, 2022, 34: 2107420
22 Feng W, Liao JF, Chang X, *et al.* Perovskite crystals redissolution strategy for affordable, reproducible, efficient and stable perovskite photovoltaics. Mater Today, 2021, 50: 199–223
23 Zhu P, Wang D, Zhang Y, *et al.* Aqueous synthesis of perovskite precursors for highly efficient perovskite solar cells. Science, 2024, 383: 524–531
24 Jeong J, Kim M, Seo J, *et al.* Pseudo-halide anion engineering for α-$FAPbI_3$ perovskite solar cells. Nature, 2021, 592: 381–385
25 Wang Y, Shi Z, Wang Y, *et al.* Intermediate phase free α-$FAPbI_3$ perovskite via green solvent assisted perovskite single crystal redissolution strategy. Adv Mater, 2023, 35: 2302298
26 Fei F, Gu L, Xu Y, *et al.* Method to inhibit perovskite solution aging: induced by perovskite microcrystals. ACS Appl Mater Interfaces, 2022, 14: 52960–52970
27 Liu Y, Zhang Y, Zhu X, *et al.* Triple-cation and mixed-halide perovskite single crystal for high-performance X-ray imaging. Adv Mater, 2021, 33: 2006010
28 Gratia P, Zimmermann I, Schouwink P, *et al.* The many faces of mixed ion perovskites: unraveling and understanding the crystallization process. ACS Energy Lett, 2017, 2: 2686–2693
29 Zhu T, Zheng D, Rager M N, *et al.* The stabilization of formamidinium lead tri-iodide perovskite through a methylammonium-based additive for high-efficiency solar cells. Sol RRL, 2020, 4: 2000348
30 Hu J, Xu Z, Murrey TL, *et al.* Triiodide attacks the organic cation in hybrid lead halide perovskites: mechanism and suppression. Adv Mater, 2023, 35: 2303373
31 Kerner R A, Schutt K, Zhu K, *et al.* $PbI_2$ reagent impurities catalyze mixed-cation halide perovskite ink degradation. ACS Energy Lett, 2022, 7: 4333–4335
32 Marchenko E I, Fateev S A, Korolev V V, *et al.* Structure-related bandgap of hybrid lead halide perovskites and close-packed $APbX_3$ family of phases. J Mater Chem C, 2022, 10: 16838–16846
33 Ding B, Ding Y, Peng J, *et al.* Dopant-additive synergism enhances perovskite solar modules. Nature, 2024, 628: 299–305
34 Dang H X, Wang K, Ghasemi M, *et al.* Multi-cation synergy suppresses phase segregation in mixed-halide perovskites. Joule, 2019, 3: 1746–1764
35 Du T, Macdonald T J, Yang R X, *et al.* Additive-free, low-temperature crystallization of stable α-$FAPbI_3$ perovskite. Adv Mater, 2022, 34: 2107850
36 Dong Q, Fang Y, Shao Y, *et al.* Electron-hole diffusion lengths >175 μm in solution-grown $CH_3NH_3PbI_3$ single crystals. Science, 2015, 347: 967–970
37 Li H, Zhang R, Li Y, *et al.* Graphdiyne-based bulk heterojunction for efficient and moisture-stable planar perovskite solar cells. Adv Energy Mater, 2018, 8: 1802012


**Acknowledgement** This work was supported by the National Natural Science Foundation of China (52102267, 22209079 and 52162028). We express our gratitude to Hongyun Chen (National Demonstration Center for Experimental Chemistry Education, Nankai University) for her assistance in testing and analyzing the ICP-OES.

**Author contributions** The manuscript was written through contributions of all authors. All authors have given approval to the final version of the manuscript.

**Conflict of interest** The authors declare that they have no conflict of interest.

**Supplementary information** Supplementary materials are available in the online version of the paper.

 © Science China Press 2024 

**Tiantian Lou** received her BE degree from Henan University of Technology in 2022. She is currently pursuing her Master's degree under the supervision of Prof. Hongshi Li at Nankai University. Her research mainly focuses on the performance optimization and precursor chemical properties of perovskite solar cells.

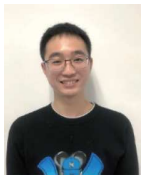

**Letian Chen** obtained his BS in materials physics from Nankai University in 2020. Currently, he is pursuing his PhD degree at Nankai University under the supervision of Prof. Zhen Zhou. His research primarily focuses on the design of electrocatalysts using computational methods and machine learning.

**Hongshi Li** has been an associate professor at Nankai University since December 2020. He earned his PhD degree from the Institute of Physics, Chinese Academy of Sciences (IOP, CAS) in the same year. His research primarily focuses on halide perovskite solar cells and single crystals.

## 揭示钙钛矿前驱体溶液的胶体组成及其对成膜的影响

娄甜甜[1†], 陈乐添[1†], 杨桂春[1], 陈鹏[1], 赵文燕[2], 李红时[1*], 李国然[1]

**摘要** 胶体是钙钛矿前驱体溶液的重要组成部分，对钙钛矿的成膜质量有重大影响. 在这项工作中, 我们探索了两种不同类型前驱体的胶体成分：原料单体混合溶解(MMD)和预合成的钙钛矿单晶再溶解(SCR). 我们发现了一种新的溶解化学平衡机制，即从混合单体到3C立方相(α相)的转变涉及一个可逆的转变过程. MMD的方法产生了多聚Pb-I溶剂化胶束，而SCR方法产生的则是六方卤化铅基的钙钛矿胶体，这种胶体组成的差别显著影响了成膜质量. 值得注意的是, 六方相胶体是有利的成核位点，可促进形成晶粒更大、相更均匀、缺陷更少的α相钙钛矿薄膜. 这项工作证明了调控胶体成分的重要性, 并从理论上深入探讨了以粉末、微晶和单晶等形式重新溶解钙钛矿的有利影响.


© Science China Press 2024